ACSNANO

www.acsnano.org

ARTICLE

A Hydrogen-Initiated Chemical Epitaxial Growth Strategy for In-Plane Heterostructured Photocatalyst

Jinqiang Zhang, Yunguo Li, Xiaoli Zhao, Huayang Zhang, Liang Wang, Haijun Chen, Shuaijun Wang, Xinyuan Xu, Lei Shi, Lai-Chang Zhang, Jean-Pierre Veder, Shiyong Zhao, Gareth Nealon, Mingbo Wu, Shaobin Wang,* and Hongqi Sun*

Cite This: https://dx.doi.org/10.1021/acsnano.0c07934

Read Online

ACCESS | Metrics & More | Article Recommendations | Supporting Information

ABSTRACT: **Integrating carbon nitride with graphene into a lateral heterojunction would avoid energy loss within the interlaminar space region on conventional composites. To date, its synthesis process is limited to the bottom-up method which lacks the targeting and homogeneity. Herein, we proposed a hydrogen-initiated chemical epitaxial growth strategy at a relatively low temperature for the fabrication of graphene/carbon nitride in-plane heterostructure. Theoretical and experimental analysis proved that methane via *in situ* generation from the hydrogenated decomposition of carbon nitride triggered the graphene growth along the active sites at the edges of confined spaces. With the enhanced electrical field from the deposited graphene (0.5%), the performances on selective photo-oxidation and photocatalytic water splitting were promoted by 5.5 and 3.7 times, respectively. Meanwhile, a 7720 μmol/h/g$_{(graphene)}$ hydrogen evolution rate was acquired without any cocatalysts. This study provides an top-down strategy to synthesize in-plane catalyst for the utilization of solar energy.**

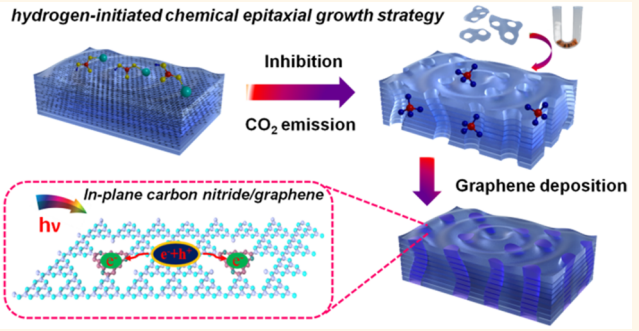

KEYWORDS: *hydrogen-initiated chemical epitaxial growth, carbon nitride/graphene, intralayer heterojunction, photocatalytic water splitting, photo-oxidation*

Carbon nitride photocatalyst with the advantages of metal-free and visible light response has been widely utilized in energy preparation,[1] pharmaceutical synthesis,[2] and environmental governance.[3] However, intrinsic carbon nitride typically suffers from inefficient generation of hot carriers, which results in low photocatalytic performance. Hybridization with graphene has been regarded as an effective approach for the modification of carbon nitride without extra addition of metal elements.[4] With a high value of charge mobility ($\mu \approx 10\,000$ cm^2/(V s)), graphene acts as an electron mediator and diverts electrons once they are excited, realizing the faster separation and transfer of charge carriers.[5,6] Nevertheless, the interlaminar space region formed in the fabricated heterojunction provides room for the relaxation of electron−hole pairs.[7] Therefore, there is still room for improvement of the photocatalytic performances of graphene/carbon nitride heterojunctions.

Inosculating carbon nitride and graphene within in-plane interfaces might hold promise to shorten the transportation path of photoinduced charge carriers in comparison to passing through the interlaminar space region in van der Waals heterojunctions.[8−10] Thus, this more rational photocatalyst in theory has always been a pursuit in the field of materials science. On the basis of this, Che et al. employed a bottom-up method to obtain (C_{ring})−C_3N_4 plane heterostructural nanosheets.[11] Despite the enhanced performance of this in-plane heterostructure, the targeting and homogeneity of formed graphene on carbon nitride substrate cannot be guaranteed. Current reasonable strategies for the fabrication of uniform intralayer heterostructures are mainly dependent on the chemical epitaxial growth (CEG) or physical vapor deposition

Received: September 21, 2020
Accepted: November 18, 2020

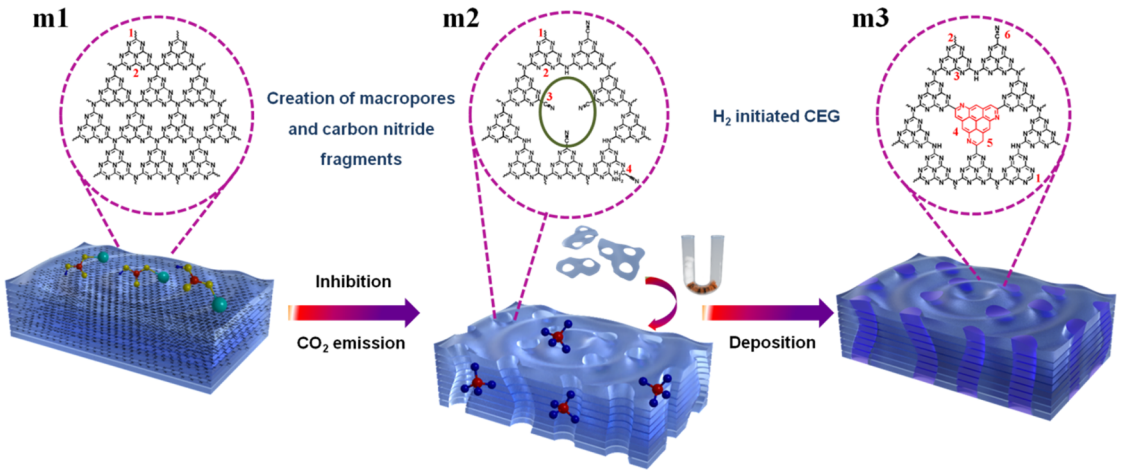

Figure 1. Schematic illustration of the formation processes of intralayer heterojunctions. m1, m2, and m3 are the proposed molecular structures of g-C_3N_4, porous carbon nitride, and hydrogenated carbon nitride, respectively.

(PVD) strategies.[8,10,12] However, reports on the fabrication of graphene/organic semiconductor intralayer heterojunctions are rare. The requirement of tremendous compatibility on the lattice constants and lattice symmetry from each component of intralayer heterostructures poses difficulties in its construction, and processing conditions such as temperature for stabilization of both sides are extremely uncontrollable.[9,10] More seriously, these requirements can not always be achieved at the same time.

Herein, we proposed a hydrogen-initiated chemical epitaxial growth strategy at a relatively low temperature for the fabrication of graphene/carbon nitride intralayer photocatalyst. Our proof-of-concept demonstration is initially on the basis of the exceptionally similar molecular configuration between carbon nitride and graphene. As demonstrated in Figure S1, both lattices of these "twisted twins" have a hexagonal symmetry with a similar space group, and the difference in each lattice parameter is only 1.4%, proving the feasibility of material construction. Moreover, considering the pyrolysis temperature of carbon nitride (starting from 600 °C) is far below the temperature for graphene formation (above 1000 °C using CVD method),[13,14] confined spaces and active sites, which are theoretical and experimental evidenced to be indispensable on graphene deposition at relatively low temperature, were created on carbon nitride substrate. After connecting the carbon rings of graphene with the tri-*s*-triazine units within carbon nitride, the acquired in-plane heterojunction was found to exhibit an enhanced electrical field and a more favorable electronic structure for facilitating carrier separation and transfer. With the trace amount of deposited graphene (0.5%), the performances on selective photooxidation and photocatalytic water splitting were increased 5.5 and 3.7 times, respectively. In particular, this in-plane heterostructure exhibited a 7720 μmol h^{-1} $g^{-1}_{(graphene)}$ hydrogen evolution rate without a noble metal as cocatalyst.

RESULTS AND DISCUSSION

The fabrication process of the graphene/carbon nitride intralayer heterojunction includes two processes (Figure 1), i.e., the creation of confined spaces with active sites at edges on bulk structure and the H_2−initiated CEG procedure for graphene formation. First, a soft template of sodium bicarbonate was added into a melamine solution followed by heating, and another molecule (Figure S2) was synthesized which was subsequently calcinated with both unreacted sodium bicarbonate and melamine. During the polymerization process, apparent pore channels were created on 10%−C_3N_4 and 14%−C_3N_4 (also named as porous carbon nitride) via the released CO_2 from the pyrolysis of sodium bicarbonate.[15] This could be confirmed from the disappeared (100) peak from XRD profiles (Figure S3) and the pores that appeared in the electron and atomic force microscopy images (Figures S4−S6). Meanwhile, with the intercalating effect of Na^+ from sodium bicarbonate,[16] a gradual decline can be observed in the (002) peak of porous carbon nitride with increasing proportions of soft template (Figure S3), which is indicative of the breaking of van der Waals bonds within the layers of bulk carbon nitride.[17] The generated molecules in the precursor contain acylamino groups at the edges (Figure S2), which could act as a polymerization inhibitor in the polymerization process of carbon nitride. Therefore, a large number of small and thin carbon nitride fragments with thicknesses less than 1 nm appeared (Figure S4c,g). These fragments can be gradually hydrogenated into methane at 500 °C in H_2 atmosphere, which cannot otherwise be achieved in N_2 (Figure S7). It is known that methane is the carbon gas source in the CEG process for graphene synthesis. Thus, the porous carbon nitride was thermally treated in hydrogen at 500 °C. After the hydrogenation process, small carbon nitride fragments disappeared and the thickness of H_2−10%−C_3N_4 and H_2−14%−C_3N_4 (also named hydrogenated carbon nitride) exhibited an improved tendency compared to that of porous carbon nitride (Figures S4d,h and S8). The same phenomenon can also be observed on transmission electron microscopy (TEM) and scanning electron microscopy (SEM) images (Figures S9 and S10), especially on H_2−14%−C_3N_4 (Figure S9d), a partial hydrogenated state where some pores were not completely patched was recorded. Therefore, we conclude that the decomposition of the small fragments in hydrogen released methane, which then *in situ* formed graphene along the edge of pores (confined spaces) to produce a unique intralayer graphene/carbon nitride heterostructure. On this occasion, the volumes of three samples, g-C_3N_4, 10%−C_3N_4, and H_2−10%−C_3N_4, at the same mass were compared (Figure S10f), revealing that the column volume of 10%−C_3N_4 significantly increased because of the exfoliation and porosity. However, the

https://dx.doi.org/10.1021/acsnano.0c07934
ACS Nano XXXX, XXX, XXX−XXX

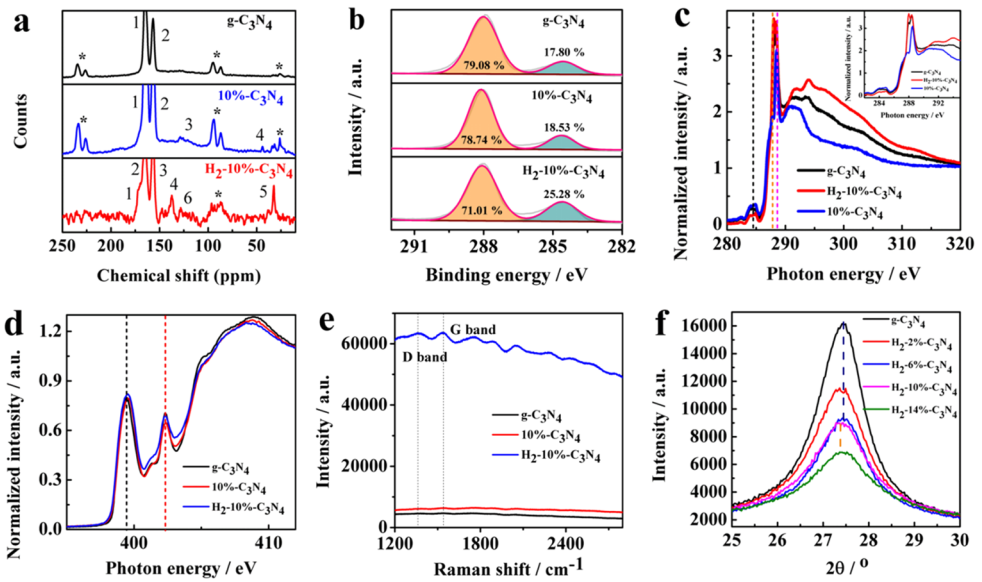

Figure 2. Microscopic evidence of the formation of graphene/carbon nitride intralayer heterojunction. (a) ^{13}C solid-state NMR spectra. (b) C 1s XPS spectra. (c, d) NEXAFS results. (e) Raman spectra. (f) Magnified XRD patterns of as-prepared samples.

volume of $H_2-10\%-C_3N_4$ decreased to almost the same as that of g-C_3N_4, indicating the loss of porosity due to the graphene filling. The same conclusion can also be reached from the BET results (Figure S11). By contrast, with less of pore maker $NaHCO_3$ in the first step of Figure 1, no obvious damage can be observed on $2\%-C_3N_4$ and $6\%-C_3N_4$, which still remained the bulk structure (Figures S5 and S6). After the calcination under H_2 atmosphere, the (002) peak intensity of both $H_2-2\%-C_3N_4$ and $H_2-6\%-C_3N_4$ (Figure S8) experienced further decrease, and their surface areas increased by 2 and 3 times, respectively, as compared with that of g-C_3N_4 (Figure S11 and Table S1). This confirms that further exfoliation, rather than the formation of graphene, occurred on $2\%-C_3N_4$ and $6\%-C_3N_4$ without confined spaces. Therefore, porous carbon nitride ($10\%-C_3N_4$ and $14\%-C_3N_4$) and hydrogenated carbon nitride ($H_2-10\%-C_3N_4$ and $H_2-14\%-C_3N_4$) will be emphasized in this work.

The microscopic changes during this modified CEG process are initially supported by the NMR spectra (Figure 2a): On pristine g-C_3N_4, two main peaks at 165 and 155 ppm are evident, corresponding to the carbon atoms at positions 1 and 2 in m1, respectively (Figure 1). In addition to these two main peaks, there is an obvious peak centered at approximately 40 ppm on porous carbon nitride, which is attributed to the CH_2 group (position 4 in m2), indicating the tri-*s*-triazine unit of the porous carbon nitride is destroyed. Besides, acylamino groups in the precursor could convert into cyano groups because of the dehydration effect during the polymerization (130 ppm in Figure 2a).[18] As a result, this damage process forms one kind of intralayer heterostructure as shown in m2. This structure is also reflected by the increased value in zeta potential of porous carbon nitride as the cyano groups have a strong electron-withdrawing ability (Table S1). While after the hydrogenation process, the signal of the CH_2 group on porous carbon nitride disappeared, with a peak emerging at 171 ppm, assigned to the methine carbon at position 1, structure m3.[19] This suggests that the damaged tri-*s*-triazine unit is repaired. Noticeably, an peak at 137 ppm associated with the sp^2 carbon also emerged, consistent with the formation of graphene during the hydrogen treatment.[20] As a result, another intralayer heterojunction connected by the *in situ* generated graphene is produced. Apart from this, a peak at 32.5 ppm was also found on $H_2-10\%-C_3N_4$, which originates from the sp^3 carbon (position 5 in m3). XPS and FTIR studies were also performed to elucidate the changes of chemical states and surface composition of the prepared samples. As observed from C 1s spectra (Figure S12), the peak at 285.4 eV assigned to amino groups on g-C_3N_4[21] shift upfield to 286 eV on $14\%-C_3N_4$ after the damage process. Meanwhile, the peak intensity gradually increases from 2.64% on g-C_3N_4 to 6.18% on $14\%-C_3N_4$, suggesting that the marginal amino groups of g-C_3N_4 gradually changed to cyano groups with the increasing amount of soft template, since cyano groups have a C 1s binding energy similar to that of amino groups.[18] This can also be proven by the FTIR spectra (Figure S13), where the peak intensity of cyano groups at 2173 cm^{-1} turns stronger and that of amino groups at 3090 cm^{-1} becomes lower with more soft template being added in the damage process.[22] Besides, it was interesting to note that the ratio between C═N and C═C bonds remained unchanged on all of the products after the damage process (Figure S12b), suggesting that no obvious changes occurred on the tri-*s*-triazine unit of the basal plane of carbon nitride. While on the hydrogenated samples, the ratio of C═C to C═N bonds rose from 0.23 in g-C_3N_4 to 0.36 in $H_2-10\%-C_3N_4$, verifying the growth of graphene (Figure 2b and S14). On the basis of the NMR, XPS, and FT-IR results, the possible molecular structures of the prepared samples are proposed in Figure 1.

The presence of graphene in the hydrogenated carbon nitride is confirmed by synchrotron-based near edge X-ray absorption fine structure (NEXAFS) spectroscopy measurements. All the samples show peaks at 284.5, 288, and 288.4 eV in C K-edge spectra (Figure 2c) which are the characteristic resonances of the defective carbon, $\pi^*_{C=C}$ and $\pi^*_{C=N-C}$, respectively.[4] For the peak at 284.5 eV, the order of intensities from low to high is $H_2-10\%-C_3N_4$, g-C_3N_4, and $10\%-C_3N_4$, indicating that more carbon defects existed in the porous carbon nitride, and following hydrogenation, some of the defects were repaired. For the peak at 288 eV, small protuberances could be observed in g-C_3N_4 and $10\%-C_3N_4$,

https://dx.doi.org/10.1021/acsnano.0c07934
ACS Nano XXXX, XXX, XXX−XXX

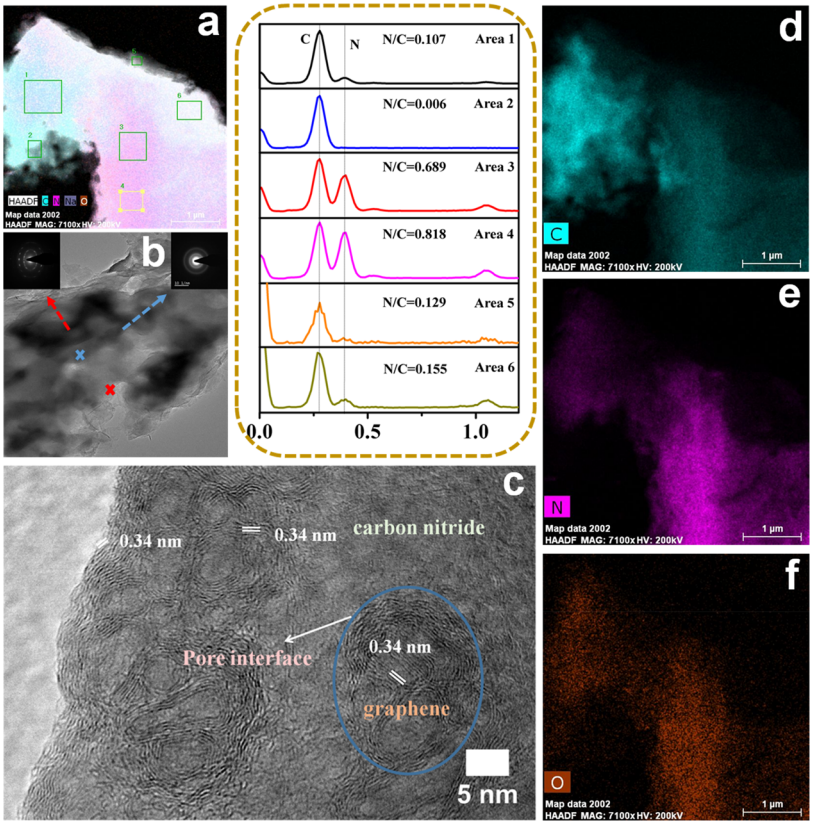

Figure 3. Macroscopic evidence of the formation of graphene/carbon nitride intralayer heterojunction. (a) High-angle annular dark-field scanning TEM images (HAADF-STEM) and corresponding EDX spectra of six areas of hydrogenated carbon nitride. Different C/N ratios in EDX spectra indicated the filling in macropores of porous carbon nitride was graphene. (b, c) HRTEM image of reconstructed carbon nitride and selected-area electron diffraction images of two different areas. (d–f) Energy-dispersive X-ray spectroscopy (EDX) elemental mapping images of hydrogenated carbon nitride.

whereas H_2−10%−C_3N_4 exhibited a single distinct peak, which demonstrates the successful deposition of the intraformational carbon ring in the basal plane of carbon nitride. In the N K-edge spectra (Figure 2d), two obvious peaks at 399.4 and 402.3 eV can be observed which are, respectively, the π^* resonances of C═N−C and C−N bonding. The reduced peak intensity at 402.3 eV on H_2−10%−C_3N_4 also confirmed that the N−3C bonding was substituted by the C═C bonding from graphene, which is consistent with the C K-edge results. The same conclusion can also be drawn from Raman spectroscopy. As shown in Figure 2e, distinct peaks of D (1370 cm^{-1}) and G (1540 cm^{-1}) bands can be seen on H_2−10%−C_3N_4 which are not evident in the graphitic carbon nitride and 10%−C_3N_4 samples, indicating the existence of graphitic carbon and defective carbon (mainly N doped carbon).[23] Besides, in XRD profiles, although the intensity of the (002) peaks in hydrogenated carbon nitride exhibited increasing tendency compared with that of porous carbon nitride (Figure S8), the (100) peaks also fail to re-emerge, confirming the absence of the CN polymer in the filled macropores of porous carbon nitride. More importantly, the (002) peaks of H_2−10%−C_3N_4 and H_2−14%−C_3N_4 shift slightly from 27.4° in g-C_3N_4 to 27.3° (Figure 2f), indicating the existence of carbon in the inplanar of carbon nitride.[24] These combined results clearly show the derivation of g-C_3N_4 structure in the modified CEG processes, in which graphene grows along the edge plane of porous carbon nitride from methane via hydrogenation of carbon nitride fragments.

Furthermore, different from the porous sample (Figure S15), uneven distributions of C and N elements on H_2−10%−C_3N_4 are evident, and carbon-rich areas are easily discernible (Figure 3). Correspondingly, in EDX spectra some areas of H_2−10%−C_3N_4 obey the same C/N ratio as that in the porous carbon nitride and some areas contain less N. The high-resolution TEM images (Figures 3c and S16) confirm an interlayer crystal lattice in hydrogenated carbon nitride which locates within the position of macropore in porous carbon nitride. The lattice spacing is 3.40 Å[12] and obvious boundaries (blue cycle in Figure 3c) can be found between carbon nitride and graphene, indicating that carbon grows along the cyclic edge of macropores on the porous carbon nitride. In addition, the selected-area electron diffraction image (inset of Figure 3b) proves the presence of in-planar order of carbon and amorphous carbon nitride. These results further confirm that the uniform graphene/carbon nitride intralayer heterojunction was obtained.

Graphitic carbon nitride (bulk nanostructure), 2%−C_3N_4 and 6%−C_3N_4 (with bulk structure and cyano groups at edge), and urea-derived carbon nitride (porous without cyano groups) were selected as contrast samples but failed to obtain graphene (Figure S17). Therefore, nanopores (confined spaces) and cyano groups at edge (active site) together are crucial factors for graphene deposition at relatively low temperatures. The reaction rates on a planar solid surface in open space and that on the solid walls within a nanopores (Figure 4a) were compared. On the basis of the collision

https://dx.doi.org/10.1021/acsnano.0c07934
ACS Nano XXXX, XXX, XXX−XXX

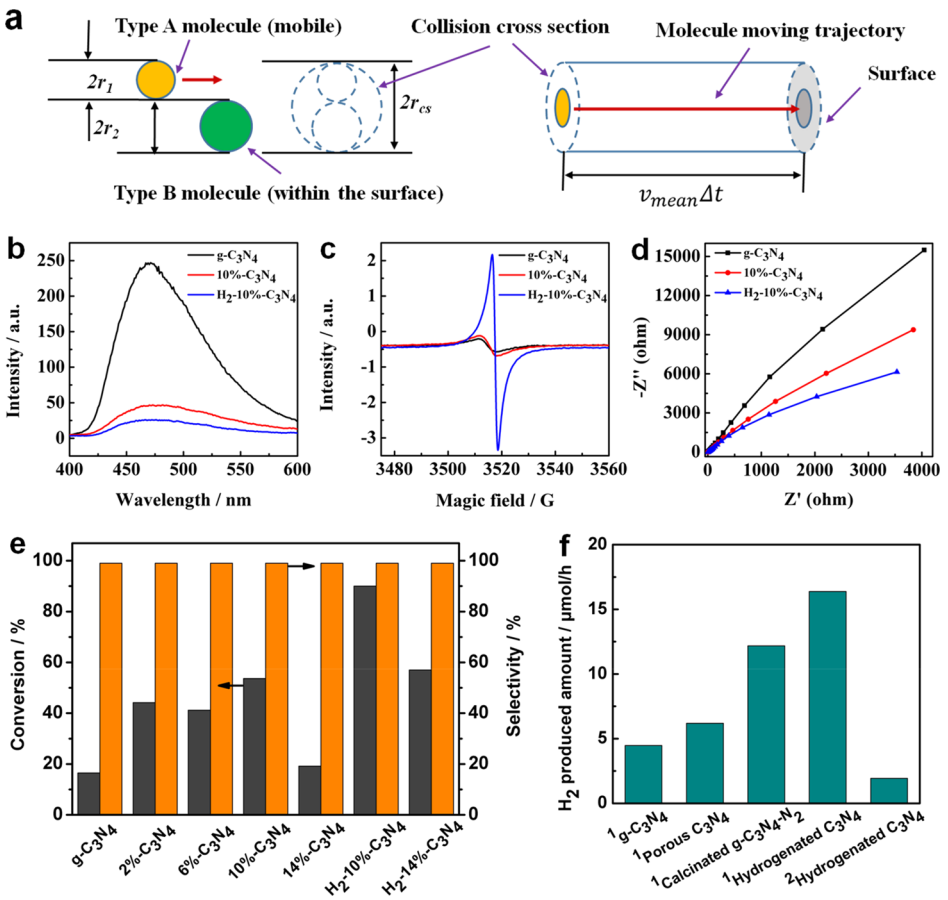

Figure 4. (a) Schematic graph of the collision process between a type A and B molecules, with collision cross section and pathway distance demonstrated. (b) Fluorescence spectrum (PL). (c) Solid ESR spectra. (d) EIS spectra. (e) Selective photo-oxidation performances. (f) Photocatalytic performances on water splitting using the prepared samples. Photocatalytic reaction conducted (1) with >420 nm filter and Pt as cocatalyst and (2) without the filter and cocatalyst.

theory shown in eq 1,[25] the reaction rate of graphene growth is directly proportional to the collision frequency.

$$r(T) = Z_\rho \exp\left(\frac{-E_a}{RT}\right) \quad (1)$$

where Z is the collision frequency, E_a represents activation energy, and R and T are the gas constant and temperature, respectively. In our case, the reaction is between a diluted gaseous phase and the reaction sites containing reactant B embedded in a solid surface. Considering a diluted gaseous reactant A moved within the vicinity (one mean free path distance to) of a solid surface where reactant B sites were embedded within a solid planar wall in open space, with all A molecules moving perpendicularly toward the surface. A collision between the A molecule and the wall will be likely to happen when the molecule is within the range of a mean free path to the wall, which will result in a reaction when a type B molecule is simultaneously within a sphere of diameter $r_{cs} = r_1 + r_2$ along the trajectory of the A molecule, where the radii of molecule A and B are respectively r_1 and r_2, and r_{cs} represents the radius of the collision cross section (Figure 4a). Within the time interval Δt, the distance traveled by the molecule A is $v_{mean}\Delta t$, while the total number of A molecules enclosed within the pathway of the cross section is $n_{+x} = Nv_{mean}\Delta t\pi r_{cs}^2/6$, where N is the number of molecules A per volume, and v_{mean} represents the mean of the Maxwell−Boltzmann velocity distribution of type A molecules. The reason for a denominator of 6 being included is that the molecules movement in a 3D space may be decomposed with respect to a Cartesian coordinate system along 6 directions, e.g., $\pm x$, $\pm y$, and $\pm z$, and that for a medium in equilibrium the number of molecules moving along the $+x$-direction will be equal.

The collision frequency on a planar wall in open space can now be calculated as the ratio of the total number of the type A molecules moving toward the wall over the length of the pathway:

$$Z_{wall} = \frac{n_{+x}}{v_{mean}\Delta t} = \frac{Nv_{mean}\Delta t\pi r_{cs}^2/6}{v_{mean}\Delta t} = \frac{N}{6}\pi r_{cs}^2 \quad (2)$$

In contrast, with a nanopore with a diameter, D, of the same order of magnitude with the mean free path λ of the type A molecules, the situation is dramatically different even assuming other conditions are unchanged. Here the geometrical constrain plays a key role, which affects the molecules moving along 4 out of the 6 directions ($\pm x$ and $\pm y$). In this case, a fraction of the molecules currently moving in these 4 directions will strike into the wall of the nanopore within a single cycle along the path way before the next collision occurs. A comparative illustration between a large pore (or a planar surface in open space) and a nanopore is given in Figure S18a,b. The quantitative expression of the collision frequency with a nanopore can then be given below.

https://dx.doi.org/10.1021/acsnano.0c07934
ACS Nano XXXX, XXX, XXX−XXX

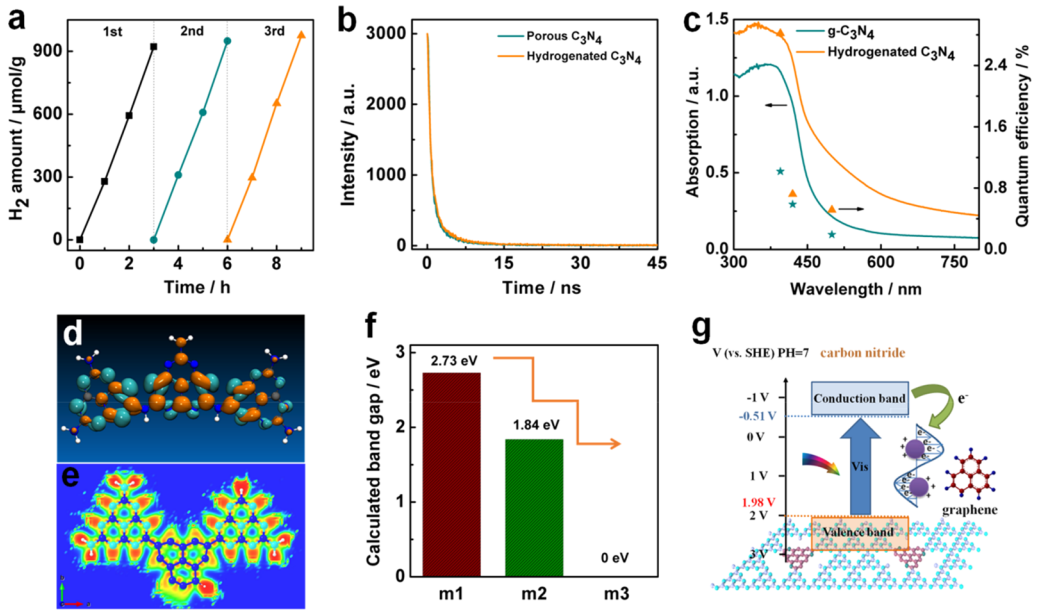

Figure 5. (a) Stability of hydrogenated carbon nitride in photocatalytic water splitting reaction with three cycles. (b) Time-resolved decay spectra of samples before and after the graphene deposition. (c) Wavelength dependent on quantum efficiency of g-C_3N_4 and hydrogenated C_3N_4. (d) DFT calculation of g-C_3N_4 unit. (e) Electron localization function of hydrogenated carbon nitride; blue, white, and cyan atoms represent carbon, hydrogen, and nitrogen, respectively. (f) Calculated band gap of corresponding modellings of g-C_3N_4, porous carbon nitride, and hydrogenated carbon nitride. (g) Diagram of electron transportation path in graphene/carbon nitride intralayered heterojunction.

$$Z_{\text{pore}} = \frac{n_{+x} + n_{-x} + n_{+y} + n_{-y}}{v_{\text{mean}}\Delta t} = \frac{4Nv_{\text{mean}}\Delta t\pi r_{\text{cs}}^2/6}{v_{\text{mean}}\Delta t} = \frac{2N}{3}\pi r_{\text{cs}}^2 \quad (3)$$

Herein, a 4-fold increase in the collision frequency, and hence also in the reaction rate, would be expected. In the case of this study, the typical nanopore diameter is ~50 nm, which is compared to the molecule mean free path in the air under standard pressure of 58 nm.[26] Then, a significant increase in both collision frequency and the reaction rate inside the nanopore is expected, compared to that on a planar surface in open space. Besides, it has been reported that the dissociation energy for a H−N bond is 386 kJ/mol,[27] while the energy required for break one of the three bonds is 355.3 kJ/mol,[28] with the latter being about 10% lower than the former. Therefore, the cyano groups at the edge of nanopores would also provide deposition sites for carbon free radical. Totally, combined with the advantages from confined spaces and cyano groups, intralayered graphene/carbon nitride heterojunction via CEG process at low temperatures could be successfully obtained.

After inserting nanographene into the lateral plane of carbon nitride, the light-response ability was improved. As shown in the UV−vis spectra (Figure S19a), g-C_3N_4 and 10%−C_3N_4 are impeded by the weak light harvesting with almost no light response when the wavelength is beyond 500 nm, while on H_2−10%−C_3N_4 an obvious improvement could be observed in the full visible region. Even in the NIR region, this intralayered heterojunction still has a response. This enhancement is precisely attributed to the plasmonic effect of incorporated nanographene.[29] On this occasion, a photo-to-thermal experiment under inert atmosphere was conducted to prove the effect of added plasmonic nanographene (Figure S19b). The temperature of g-C_3N_4 can increase to 97 °C within 30 min light irradiation mostly due to the heat dissipation from the recombination of photoinduced charge carriers, while after adding a trace amount (0.5%) of nanographene into the basal plane of carbon nitride (Table S2), the temperature is sharply increased to 118 °C, which is comparable to that of graphene with same mass. Excluding the heat generated from the recombination of photoinduced electron−hole pairs on carbon nitride, the extra elevated temperature on the hydrogenated carbon nitride (more than 20 °C) confirms the enhanced electrical field on the graphene/carbon nitride heterojunction.[30,31] Moreover, the enhancement after the addition of graphene into the confined spaces of carbon nitride was also verified using the finite element method. Embedding graphene nanocolumns into the confined spaces of porous carbon nitride has a dramatic impact over the original homogeneous electrical field (E) distribution (Figures S19 and S20). High field concentration is observed around the edge of the graphene nanocolumn. The electrical field is plotted along a horizontal line, drawn around the top right corner of the graphene columns where the local field maximum is found. A comparison is made between local intensity at the maximum on the heterostructure and that on the plain g-C_3N_4 with the ratio $I/I_0 = (E/E_0)^2$ being plotted in Figure S19c. The enhancement ripples the full spectrum and is wavelength-dependent. This observation is similar to the situation when metal nanoparticals (NPs) are setting on semiconductor substrate.[32]

The separation rate of electron−hole pairs of carbon nitride is also boosted as a result of surrounded electrical field from plasmonic nanographene. Indeed, the intensity of the PL peak at 470 nm on porous carbon nitride reduced (Figures 4b and S21) and the intensity of the ESR characteristic peak of the unpaired electrons on the carbon nitride units rose (Figure 4c), both indicating the recombination of photoinduced charge

https://dx.doi.org/10.1021/acsnano.0c07934
ACS Nano XXXX, XXX, XXX−XXX

carriers was effectively prohibited after the addition of nanographene.[33] Furthermore, the heterojunction exhibited a less interfacial electron resistance due to the high electroconductibility of graphene (Figure 4d).

With suitable band structures (Figures S22−S24 and Table S1) and an enhanced electrical field, the as-obtained carbon nitride sample was then evaluated for photoinduced selective oxidation of 1,4-dihydro-2,6-dimethylpyridine-3,5-dicarboxylate (1,4-DHP) (Figure S25−27).[22,34] Pristine carbon nitride exerted a low conversion of 1,4-DHP (Figure 4e and Table S3) due to the weak light-response ability and constraint of the Coulomb force for charge carriers. Once the bulk carbon nitride was damaged to create the intralayer heterojunction at the edge plane of macropores, the photo-oxidation rate of 1,4-DHP increased by almost 3-fold on 10%−C_3N_4 with a conversion rate of 53.7%. The conversion rate for photo-oxidation of 1,4-DHP experienced a significant enhancement after introducing only 0.5% plasmonic nanographene onto carbon nitride intralayer, with 5.5 times improvement on H_2−10%−C_3N_4 compared to g-C_3N_4. The prepared samples were also used for photocatalytic hydrogen evolution, and activity was acquired on hydrogenated carbon nitride which was 3.7 times that of g-C_3N_4 (Figure 4f). Meanwhile, hydrogenated carbon nitride showed a satisfied stability without any decrease on photocatalytic hydrogen evolution ability after three cycle (Figure 5a). In particular, the metal-free photocatalyst still exhibited photocatalytic ability on water splitting in the absence of cocatalyst, with a hydrogen evolution rate of 7720 μmol/h/$g_{graphene}$ under light irradiation without >420 nm filter, which is higher than reported carbon/carbon nitride composites (Table S4). As re-sintering of carbon nitride resulted in the interlayer stripping, the influence of heating under N_2 rather than hydrogen atmosphere on the carbon nitride was also studied. The photocatalytic hydrogen evolution rate of calcinated g-C_3N_4−N_2 was 12.2 μmol/h, which was lower than that of hydrogenated carbon nitride (16.4 μmol/h; Figure 4f), suggesting that the self-assembly of nanographene into carbon nitride is more efficient for the catalyst modification. Furthermore, the time-resolved decay spectra of samples before and after the graphene deposition were obtained for confirming the enhanced performance. As shown in Figure 5b and Table S5, the average lifetime of hydrogenated carbon nitride was 2.14 ns, which was longer than the sample before the graphene deposition (1.99 ns). Meanwhile, a visible-light-irradiated photocurrent was obtained in H_2−10%−C_3N_4 that was higher than that in g-C_3N_4 and 10%−C_3N_4, further demonstrating the higher efficiency in the separation of photoinduced charge carriers on the advanced metal-free photocatalyst (Figure S28). As a result, the quantum efficiency of hydrogenated carbon nitride at 395, 420, and 500 nm were all higher than that of g-C_3N_4 (Figure 5c).

The improvement on light absorption and photocatalytic performances after the graphene formation was proven by DFT calculations (Figure 5d−f), in which part of m1 (Figure 5d), m2 (Figure S29b), and m3 (Figure 5e) molecules are employed as they represent the characteristics of the corresponding samples and are able to affect the optical and electrochemical properties of the relevant intact structures. The porous carbon nitride and hydrogenated carbon nitride presented lowered band gap energies by comparison to g-C_3N_4. In particular, the m3 structure exhibited partial metallicity with band gap 0 eV, demonstrating the enhanced optical property of H_2−10%−C_3N_4. To unveil the effect of the fabricated heterostructure on the electronic structure of carbon nitride, frontier molecular orbitals were examined (Figure 5 and Figure S29). With the g-C_3N_4 system, the LUMO is mainly consisted of C−N bonding orbitals and HOMO is derived from the heterocyclic nitrogen p_z orbitals.[34] On the porous carbon nitride system, the LUMO shifts from the melem to the damaged unit, while the HOMO mainly locates on the melem moiety, indicative of promoted separation of charge carriers. After incorporation of the carbon ring into hydrogenated carbon nitride, the electrons between some of the C═C bonding of carbon rings were not well localized and exhibited partial metallization. As the partial metallization of the joint on intralayer heterojunction enabled more free electrons to assemble, enhanced electrical field could be obtained on this area. These results are consistent with that calculated by FE method. As a result of combined DFT and FE calculations, the conclusion could be reached that the heterostructure of obtained photocatalyst enhances the electrical field which compels the charge carriers out of the constraint of the Coulomb force and that the formed graphene acts as the transferring channel of photoinduced electron, both effectively prohibiting the recombination of electron/hole pairs for redox reactions (Figure 5g).

CONCLUSIONS

In summary, we proposed a hydrogen-initiated chemical epitaxial growth strategy to fabricate intralayered polymer-based heterojunction. Compared with the traditional CVD method, this strategy can be realized at relatively low temperatures as a result of the confined space and active site. Combined the experimental and computational methods, the acquired in-plane heterojunction exhibits enhanced electrical field and a more efficient electronic structure to facilitate carriers' separation and transfer. As a result, this photocatalyst is shown to possess better performances on artificial synthesis. This work is expected to shed light in further improvement of CEG process for constructing metal-free photocatalysts in order to achieve feasible photosynthesis.

METHODS

Damage of Bulk Structured Carbon Nitride. Porous carbon nitride was prepared by a soft template method. Typically, 5 g of melamine and sodium bicarbonate (the mass varied from 0.1 to 0.3, 0.5, and 0.7 g to respectively synthesize 2%−C_3N_4, 6%−C_3N_4, 10%−C_3N_4, and 14%−C_3N_4) were both dissolved in ultrapure water and subsequently heated at 100 °C for water evaporation. After that, the obtained precursor was fully ground with an agate mortar and put into a furnace. Heat treatment of the precursor was done at 823 K for 4 h with a heating rate of 2.3 K min^{-1}. After the calcination, the samples were thoroughly washed by hot water and ethanol for several times and subsequently dried at 333 K overnight to obtain the porous carbon nitride. For comparison, a sample of bulk g-C_3N_4 was synthesized by the same synthesis procedure without using the soft template of sodium bicarbonate.

Modified Chemical Epitaxial Growth Strategy for Graphene/Carbon Nitride Intralayered Heterojunctions. Initially, a certain amount of the prepared porous carbon nitride was put into a quartz U-tube which was then put into a temperature-programmed heating jacket. The U-tube was degassed at 523 K with N_2 for 2 h. Then the gas was changed to H_2/N_2 mixture with the concentration of H_2 5%, and the degassed sample was heated to 773 K at a heating rate of 5 K/min. After the temperature arrived at 773 K, it was naturally cooled to room temperature to obtain the hydrogenated carbon nitride. The influence of heating under inert gas rather than

https://dx.doi.org/10.1021/acsnano.0c07934
ACS Nano XXXX, XXX, XXX−XXX

hydrogen atmosphere on the carbon nitride was also studied with the same reaction condition but the hydrogen atmosphere was replaced by the ultrapure nitrogen. The obtained sample was named as calcinated g-C_3N_4–N_2.

Characterizations. The structures of the prepared photocatalysts were characterized through the X-ray diffraction (X'Pert PRO MPD, Holland). N_2 adsorption–desorption isotherms were obtained from a Micromeritics Tristar 3000 at 77 K. SEM images were captured on a FEI Verios XHR 460. TEM and HRTEM images were recorded on a JEOL 2100. HAADF-STEM and EDX elemental mapping were performed by a FEI Titan G2 80–200 TEM/STEM. XPS measurements were performed using a Kratos Axis Ultra DLD spectrometer with an Al Kα (1486 eV) X-ray source operating at 225 W. Survey spectra were obtained employing a pass energy of 160 eV, while all high-resolution spectra was collected via a pass energy of 40 eV. The binding energy scale of all XPS spectra were calibrated by locking the C 1s peak to 284.5 eV. NEXAFS tests were carried out with the Soft X-ray beamline from the Australian Synchrotron[35] and conducted at room temperature under the condition of ultrahigh vacuum (UHV). All spectra were collected in the partial electron yield (PEY) mode using an electron flood gun to adequately neutralize the sample. The normalizing of all the NEXAFS spectra was processed with the QANT software program developed by the Australian Synchrotron.[36] AFM images were collected by a Bruker icon equipment. Solid-state ^{13}C direct polarization (DP) and cross-polarization (CP) MAS NMR spectra were obtained on a Varian VNMRS WB spectrometer (^1H 399.868 MHz, ^{13}C 100.554 MHz) equipped with a 4 mm MAS probe. All samples were spun at 7 kHz in 4 mm zircon rotors with kel-F caps. A 90° pulse of 5 us, contact time of 2 ms (CP-MAS) and recycle times of 2 and 60 s were used for the CP-MAS and DP-MAS experiments, respectively. For all experiments, 1000 data points were collected and zero-filled to 8000 points, with a line broadening of 100 Hz applied. Chemical shifts were determined against an external adamantine standard (38.5 ppm) and are reported relative to tetramethylsilane (0 ppm). Fourier transform infrared (FT-IR) spectra were collected on a PerkinElmer instrument. Diffuse reflectance spectra and photoluminescence spectra (PL) were recorded on a Cary 100 UV–vis Spectrophotometer and a Cary Eclipse Fluorescence Spectrophotometer (Agilent), respectively. The time-resolved decay spectra were performed on a FLS1000 with the excitation and detection wavelengths were 375 and 460 nm, respectively.

***In Situ* Detection of Effluent Gases under H_2 or N_2 Calcination.** Porous carbon nitride was placed in a sealed tube furnace, which was connected with an on-line gas chromatograph (GC, Agilent 7820A). H_2 or N_2 was purged into the reactor to fully replace the air inside. Then the furnace was heated and the effluent gases were analyzed by gas chromatograph equipped with Porapak N and Molsieve 5A columns.

Photoinduced Selective Oxidation of 1,4-DHP. The photooxidation tests were conducted in a customized reactor. The aqueous solution (50 mL) dispersing 10^{-4} mol/L 1,4-DHP and samples (30.0 mg) was irradiated by a LED solar simulator (Newport). After 1 h, the conversion of 1,4-DHP was monitored by a Cary 100 UV–vis spectrophotometer.

Photocatalytic Water Splitting. The H_2 evolution tests were performed by using a LabSolar-III AG reaction system (Beijing PerfectLight Co.). Photocatalyst (50 mg) was dispersed into a 50 mL of aqueous solution containing 5 mL of TEOA and 0.8 mL $H_2PtCl_6 \cdot (H_2O)_6$ (3.0 wt %). Before the irradiation, the reaction cell was sealed to thoroughly evacuate for 40 min to remove air. A Xe lamp (300 W) (CEL-HXF300, Beijing Cel Sci-tech Co., Ltd.) equipped with a 420 nm cutoff filter was employed as the visible light source. The reaction system was kept at 6 °C using the cooling water. The generated hydrogen was detected with an on-line GC (GC7920) equipped with a 5 Å molecular sieve column and a thermal conductive detector (TCD). N_2 was employed as the carrier gas. Same reactions without $H_2PtCl_6 \cdot (H_2O)_6$ as cocatalyst and without cutoff filter were also performed. Besides, the stability of hydrogenated carbon nitride was studied in the water-splitting reaction with three cycles. In addition, the quantum efficiency of photocatalytic water splitting reaction was tested under the irradiations of monochromatic light including 395, 420, and 500 nm.

Photo-to-Thermal Tests. A 50 mg sample was dispersed uniformly on a quartz microfiber filter which was sealed in a quartz reactor. A thermocouple was contacted with the surface of filter for monitoring the temperature of sample. Before reaction, the reactor was replaced by Ar for 2 h to make sure no air inside. Then light with 1 W/cm^2 was irradiated on the sample and simultaneously the temperature of sample was recorded at certain time intervals.

Simulation Details. Vienna Ab initio Simulations Package (VASP) was used to perform the DFT simulations.[37,38] The projected augmented wave (PAW) method and generalized gradient approximation (GGA) in the Perdew, Burke, and Ernzerhof (PBE)[39] parametrization were used. The molecule fragments were modeled in a 35 × 18 × 15 Å^3 supercell, which allows at least a distance of 10 Å between images in any dimension. The first Brillouin zone was sampled by using a gamma-centered *k*-point set of 1 × 2 × 2. The plane-wave cutoff energy was set at 400 eV. The coordinates were fully relaxed, and the energy and force were converged within 10^{-4} eV/cell and 10^{-2} eV/Å, respectively.

The finite element modeling (FEM) on the basis of classical electro-magnetic field theory was employed to obtain the electrical field by solving Maxwell equations. COMSOL Multiphysics software[40] was used for modeling the plasmonic effect within the carbon nitride/graphene structure. The size of the simulation domain was of the same order of magnitude with the optical wavelength, so the effect of the wavelength variation can be accurately evaluated. A FEM model is constructed with the upper part of the domain filled with water, while the lower part is filled with the g-C_3N_4 materials, separated by a horizontal boundary. A graphene column with a diameter of 50 nm is embedded at the center of g-C_3N_4 material. For comparison purpose the second model of plain g-C_3N_4 block was built. Perfect matching layers (PMLs) were defined both at the top and at the bottom of the model, which were designed to completely absorb all the reflected and transmitted waves with arbitrary wave front, respectively, so as to remove any interference of back-reflected waves from the top and bottom. For all of the FEM modeling results presented in this work, an incident radiation is set at the top, transmitting downward with an intensity of 10^4 W/m^2.

ASSOCIATED CONTENT

Supporting Information

The Supporting Information is available free of charge at https://pubs.acs.org/doi/10.1021/acsnano.0c07934.

Experimental details, textural properties, chemical compositions, TEM, SEM and AFM images, FT-IR, nitrogen isotherms, XPS-VB, photo-oxidation performances of 1,4-DHP, photocurrent curves, FEM and DFT simulations (PDF)

AUTHOR INFORMATION

Corresponding Authors

Hongqi Sun – *School of Engineering, Edith Cowan University, Joondalup, Western Australia 6027, Australia;* orcid.org/0000-0003-0907-5626; Email: h.sun@ecu.edu.au

Shaobin Wang – *School of Chemical Engineering, The University of Adelaide, Adelaide, SA 5005, Australia;* orcid.org/0000-0002-1751-9162; Email: shaobin.wang@adelaide.edu.au

Authors

Jinqiang Zhang – *School of Engineering, Edith Cowan University, Joondalup, Western Australia 6027, Australia*

Yunguo Li – *Department of Earth Sciences, University College London, London WC1E 6BT, United Kingdom;* orcid.org/0000-0002-6221-7585

https://dx.doi.org/10.1021/acsnano.0c07934
ACS Nano XXXX, XXX, XXX–XXX

Xiaoli Zhao − *School of Engineering, Edith Cowan University, Joondalup, Western Australia 6027, Australia*
Huayang Zhang − *School of Chemical Engineering, The University of Adelaide, Adelaide, SA 5005, Australia*
Liang Wang − *State Key Laboratory of Mater-Oriental Chemical Engineering, College of Chemistry and Chemical Engineering, Nanjing Tech University, Nanjing 210009, China*
Haijun Chen − *Jiangsu Key Laboratory of Process Enhancement and New Energy Equipment Technology, Jiangsu Engineering Laboratory of Energy Conservation and Environmental Protection Technologies and Equipment in Process Industry, School of Mechanical and Power Engineering, Nanjing Tech University, Nanjing 211816, China*
Shuaijun Wang − *School of Engineering, Edith Cowan University, Joondalup, Western Australia 6027, Australia*
Xinyuan Xu − *School of Engineering, Edith Cowan University, Joondalup, Western Australia 6027, Australia*
Lei Shi − *School of Engineering, Edith Cowan University, Joondalup, Western Australia 6027, Australia*
Lai-Chang Zhang − *School of Engineering, Edith Cowan University, Joondalup, Western Australia 6027, Australia;* orcid.org/0000-0003-0661-2051
Jean-Pierre Veder − *John de Laeter Centre, Curtin University, Perth, Western Australia 6102, Australia*
Shiyong Zhao − *Fuels and Energy Technology Institute & Western Australia School of Mines: Minerals, Energy and Chemical Engineering, Curtin University, Perth, Western Australia 6102, Australia*
Gareth Nealon − *Centre for Microscopy, Characterisation and Analysis, The University of Western Australia, Crawley, Western Australia 6009, Australia*
Mingbo Wu − *State Key Laboratory of Heavy Oil Processing, Institute of New Energy, College of Chemical Engineering, China University of Petroleum (East China), Qingdao 266580, China;* orcid.org/0000-0003-0048-778X

Complete contact information is available at: https://pubs.acs.org/10.1021/acsnano.0c07934

Author Contributions

The manuscript was written through contributions of all authors. All authors have given approval to the final version of the manuscript.

Notes

The authors declare no competing financial interest.

ACKNOWLEDGMENTS

H.S. expresses his thanks for the support from ECU Vice-Chancellor's Professorial Research Fellowship. This work was partially supported by the Australian Research Council (DP170104264 and DP190103548). The authors acknowledge assistance from the Centre for Microscopy, Characterisation and Analysis of the University of Western Australia and the WA X-ray Surface Analysis Facility of Curtin University, funded by an Australian Research Council LIEF grant (LE120100026). The authors are also grateful for the valuable advice and technical support provided by B. Cowie and L. Thompsen regarding NEXAFS tests. All NEXAFS measurements were conducted on the soft X-ray beamline of the Australian Synchrotron, Victoria, Australia, part of ANSTO.

REFERENCES

(1) Shoji, S.; Peng, X.; Yamaguchi, A.; Watanabe, R.; Fukuhara, C.; Cho, Y.; Yamamoto, T.; Matsumura, S.; Yu, M.-W.; Ishii, S.; Fujita, T.; Abe, H.; Miyauchi, M. Photocatalytic Uphill Conversion of Natural Gas beyond the Limitation of Thermal Reaction Systems. *Nat. Catal.* **2020**, *3*, 148−153.
(2) Fu, M.; Shang, R.; Zhao, B.; Wang, B.; Fu, Y. Photocatalytic Decarboxylative Alkylations Mediated by Triphenylphosphine and Sodium Iodide. *Science* **2019**, *363*, 1429−1434.
(3) Sun, H.; Zhou, G.; Wang, Y.; Suvorova, A.; Wang, S. A New Metal-Free Carbon Hybrid for Enhanced Photocatalysis. *ACS Appl. Mater. Interfaces* **2014**, *6*, 16745−16754.
(4) Zheng, Y.; Jiao, Y.; Zhu, Y.; Li, L. H.; Han, Y.; Chen, Y.; Du, A.; Jaroniec, M.; Qiao, S. Z. Hydrogen Evolution by a Metal-Free Electrocatalyst. *Nat. Commun.* **2014**, *5*, 3783−3791.
(5) Yu, Q.; Jauregui, L. A.; Wu, W.; Colby, R.; Tian, J.; Su, Z.; Cao, H.; Liu, Z.; Pandey, D.; Wei, D.; Chung, T. F.; Peng, P.; Guisinger, N. P.; Stach, E. A.; Bao, J.; Pei, S.-S.; Chen, Y. P. Control and Characterization of Individual Grains and Grain Boundaries in Graphene Grown by Chemical Vapour Deposition. *Nat. Mater.* **2011**, *10*, 443−449.
(6) Kim, H.; Miura, Y.; Macosko, C. W. Graphene/Polyurethane Nanocomposites for Improved Gas Barrier and Electrical Conductivity. *Chem. Mater.* **2010**, *22*, 3441−3450.
(7) Zhou, P.; Yu, J.; Jaroniec, M. All-Solid-State Z-Scheme Photocatalytic Systems. *Adv. Mater.* **2014**, *26*, 4920−4935.
(8) Liu, L.; Park, J.; Siegel, D. A.; McCarty, K. F.; Clark, K. W.; Deng, W.; Basile, L.; Idrobo, J. C.; Li, A. P.; Gu, G. Heteroepitaxial Growth of Two-Dimensional Hexagonal Boron Nitride Templated by Graphene Edges. *Science* **2014**, *343*, 163−167.
(9) Liu, Z.; Ma, L.; Shi, G.; Zhou, W.; Gong, Y.; Lei, S.; Yang, X.; Zhang, J.; Yu, J.; Hackenberg, K. P.; Babakhani, A.; Idrobo, J. C.; Vajtai, R.; Lou, J.; Ajayan, P. M. In-Plane Heterostructures of Graphene and Hexagonal Boron Nitride with Controlled Domain Sizes. *Nat. Nanotechnol.* **2013**, *8*, 119−124.
(10) Liu, Y.; Huang, Y.; Duan, X. Van der Waals Integration before and beyond Two-Dimensional Materials. *Nature* **2019**, *567*, 323−333.
(11) Che, W.; Cheng, W.; Yao, T.; Tang, F.; Liu, W.; Su, H.; Huang, Y.; Liu, Q.; Liu, J.; Hu, F.; Pan, Z.; Sun, Z.; Wei, S. Fast Photoelectron Transfer in (Cring)-C_3N_4 Plane Heterostructural Nanosheets for Overall Water Splitting. *J. Am. Chem. Soc.* **2017**, *139*, 3021−3026.
(12) Huang, C.; Chen, C.; Zhang, M.; Lin, L.; Ye, X.; Lin, S.; Antonietti, M.; Wang, X. Carbon-Doped BN Nanosheets for Metal-Free Photoredox Catalysis. *Nat. Commun.* **2015**, *6*, 7698−7705.
(13) Cai, Z.; Liu, B.; Zou, X.; Cheng, H. M. Chemical Vapor Deposition Growth and Applications of Two-Dimensional Materials and Their Heterostructures. *Chem. Rev.* **2018**, *118*, 6091−6133.
(14) Li, H.; Li, Y.; Aljarb, A.; Shi, Y.; Li, L.-J. Epitaxial Growth of Two-Dimensional Layered Transition-Metal Dichalcogenides: Growth Mechanism, Controllability, and Scalability. *Chem. Rev.* **2018**, *118*, 6134−6150.
(15) Tian, W.; Zhang, H.; Sun, H.; Suvorova, A.; Saunders, M.; Tade, M.; Wang, S. Heteroatom (N or N-S)-Doping Induced Layered and Honeycomb Microstructures of Porous Carbons for CO_2 Capture and Energy Applications. *Adv. Funct. Mater.* **2016**, *26*, 8651−8661.
(16) Tang, H.; Xiong, F.; Jiang, Y.; Pei, C.; Tan, S.; Yang, W.; Li, M.; An, Q.; Mai, L. Alkali Ions Pre-Intercalated Layered Vanadium Oxide Nanowires for Stable Magnesium Ions Storage. *Nano Energy* **2019**, *58*, 347−354.
(17) Tay, Q.; Kanhere, P.; Ng, C. F.; Chen, S.; Chakraborty, S.; Huan, A. C. H.; Sum, T. C.; Ahuja, R.; Chen, Z. Defect Engineered g-C_3N_4 for Efficient Visible Light Photocatalytic Hydrogen Production. *Chem. Mater.* **2015**, *27*, 4930−4933.
(18) Yu, H.; Shi, R.; Zhao, Y.; Bian, T.; Zhao, Y.; Zhou, C.; Waterhouse, G. I. N.; Wu, L. Z.; Tung, C. H.; Zhang, T. Alkali-Assisted Synthesis of Nitrogen Deficient Graphitic Carbon Nitride with Tunable Band Structures for Efficient Visible-Light-Driven Hydrogen Evolution. *Adv. Mater.* **2017**, *29*, 1605148−1605155.

(19) Hosmane, R. S.; Rossman, M. A.; Leonard, N. J. Synthesis and Structure of Tri-s-triazine. *J. Am. Chem. Soc.* **1982**, *104*, 5497−5499.
(20) Gao, W.; Alemany, L. B.; Ci, L.; Ajayan, P. M. New Insights into the Structure and Reduction of Graphite Oxide. *Nat. Chem.* **2009**, *1*, 403−408.
(21) Akaike, K.; Aoyama, K.; Dekubo, S.; Onishi, A.; Kanai, K. Characterizing Electronic Structure near the Energy Gap of Graphitic Carbon Nitride Based on Rational Interpretation of Chemical Analysis. *Chem. Mater.* **2018**, *30*, 2341−2352.
(22) Wu, W.; Zhang, J.; Fan, W.; Li, Z.; Wang, L.; Li, X.; Wang, Y.; Wang, R.; Zheng, J.; Wu, M.; Zeng, H. Remedying Defects in Carbon Nitride to Improve Both Photooxidation and H_2 Generation Efficiencies. *ACS Catal.* **2016**, *6*, 3365−3371.
(23) Duan, X.; O'Donnell, K.; Sun, H.; Wang, Y.; Wang, S. Sulfur and Nitrogen Co-Doped Graphene for Metal-Free Catalytic Oxidation Reactions. *Small* **2015**, *11*, 3036−3044.
(24) Guo, F.; Yang, P.; Pan, Z.; Cao, X.-N.; Xie, Z.; Wang, X. Carbon-Doped BN Nanosheets for the Oxidative Dehydrogenation of Ethylbenzene. *Angew. Chem., Int. Ed.* **2017**, *56*, 8231−8235.
(25) McNaught, A. D., Wilkinson, A. *Compendium of Chemical Terminology*; Blackwell Science: Oxford, 1997; Vol. *1669*.
(26) Jennings, S. The Mean Free Path in Air. *J. Aerosol Sci.* **1988**, *19*, 159−166.
(27) Benson, S. W. III-Bond Energies. *J. Chem. Educ.* **1965**, *42*, 502−518.
(28) Alkorta, I.; Elguero, J. Dissociation Energies and Rotational Barriers about CC Single, Double, and Triple Bonds: A Hybrid HF-DFT Approach (Becke3LYP/6-311++ G**). *Struct. Chem.* **1998**, *9*, 59−63.
(29) Meng, X.; Wang, T.; Liu, L.; Ouyang, S.; Li, P.; Hu, H.; Kako, T.; Iwai, H.; Tanaka, A.; Ye, J. Photothermal Conversion of CO_2 into CH_4 with H_2 over Group VIII Nanocatalysts: An Alternative Approach for Solar Fuel Production. *Angew. Chem., Int. Ed.* **2014**, *53*, 11478−11482.
(30) Govorov, A. O.; Zhang, H.; Demir, H. V.; Gun'ko, Y. K. Photogeneration of Hot Plasmonic Electrons with Metal Nanocrystals: Quantum Description and Potential Applications. *Nano Today* **2014**, *9*, 85−101.
(31) Aslam, U.; Chavez, S.; Linic, S. Controlling Energy Flow in Multimetallic Nanostructures for Plasmonic Catalysis. *Nat. Nanotechnol.* **2017**, *12*, 1000−1005.
(32) Liu, X.; Swihart, M. T. J. C. S. R. Heavily-Doped Colloidal Semiconductor and Metal Oxide Nanocrystals: An Emerging New Class of Plasmonic Nanomaterials. *Chem. Soc. Rev.* **2014**, *43*, 3908−3920.
(33) Zhang, J.; Zhang, G.; Chen, X.; Lin, S.; Mohlmann, L.; Dolega, G.; Lipner, G.; Antonietti, M.; Blechert, S.; Wang, X. Co-Monomer Control of Carbon Nitride Semiconductors to Optimize Hydrogen Evolution with Visible Light. *Angew. Chem., Int. Ed.* **2012**, *51*, 3183−3187.
(34) Zhang, J.; An, X.; Lin, N.; Wu, W.; Wang, L.; Li, Z.; Wang, R.; Wang, Y.; Liu, J.; Wu, M. Engineering Monomer Structure of Carbon Nitride for the Effective and Mild Photooxidation Reaction. *Carbon* **2016**, *100*, 450−455.
(35) Watts, B.; Swaraj, S.; Nordlund, D.; Luning, J.; Ade, H. Calibrated NEXAFS Spectra of Common Conjugated Polymers. *J. Chem. Phys.* **2011**, *134* (2), 024702−024717.
(36) Gann, E.; McNeill, C. R.; Tadich, A.; Cowie, B. C.; Thomsen, L. Quick AS NEXAFS Tool (QANT): A Program for NEXAFS Loading and Analysis Developed at the Australian Synchrotron. *J. Synchrotron Radiat.* **2016**, *23* (1), 374−380.
(37) Kresse, G.; Joubert, D. From Ultrasoft Pseudopotentials to the Projector Augmented-Wave Method. *Phys. Rev. B: Condens. Matter Mater. Phys.* **1999**, *59* (3), 1758−1775.
(38) Blöchl, P. E. Projector Augmented-Wave Method. *Phys. Rev. B: Condens. Matter Mater. Phys.* **1994**, *50* (24), 17953−17979.
(39) Perdew, J. P.; Burke, K.; Ernzerhof, M. Generalized Gradient Approximation Made Simple. *Phys. Rev. Lett.* **1996**, *77* (18), 3865−3868.
(40) Pryor, R. W. *Multiphysics Modeling Using COMSOL: A First Principles Approach*; Jones and Bartlett Publishers: Sudbury, MA, 2009.

https://dx.doi.org/10.1021/acsnano.0c07934
ACS Nano XXXX, XXX, XXX−XXX